Optical cross-connect system based on the White cell and three-state microelectromechanical system: experimental demonstration of the quartic cell

Víctor Argueta-Díaz and Betty Lise Anderson

We present a proof of concept (design, simulations, and experimental results) for an optical cross-connection device based on the optical White cell and a three-state microelectromechanical system tilting mirror array. We describe in detail the implementation of an underpopulated quartic White cell configuration. We discuss the aberrations associated with the output of the system.

OCIS codes: 060.4510, 230.1150.

1. Introduction

An interesting problem in optical communications is that of performing routing and cross connection in the optical domain. The bandwidth of current optical communication systems is limited by the systems' electronic parts, which prevent the use of the transmitting media at their full capacity. New architectures transparent to the bit-rate and modulation format while providing reconfiguration, scalability, and fast restoration capabilities have been investigated.[1–5]

Several approaches to optical cross connects can be found in the literature. Waveguide approaches involving electro-optic[6–8] and thermo-optic switches,[9,10] and liquid crystals[11] usually involve cascading 2×2 switches for larger numbers of inputs and outputs. The waveguide solution is limited in the number of possible ports owing to the coupling losses between each one of the 2×2 switches, and also because these approaches require all the inputs and outputs to be in a single plane; the integrated optics circuit substrates can be only so large.

Here, however, we are interested in free-space systems using microelectromechanical systems (MEMSs). The MEMS is an attractive technology that allows optical switching for a large number of ports with low loss and low cost per port.[12] In general, MEMSs optical cross-connect (OXC) solutions can be divided into two main groups: 2D digital MEMSs and 3D analog MEMSs. In 2D digital MEMSs, the switches are integrated in a two-dimensional array of micromirrors on a silicon substrate, where the beams propagate parallel to the substrate. Depending on the MEMS, the micromirrors can be tilted, rotated, or lifted into and out of the optical path to change the propagation direction of the optical beam from a particular input.[13,14]

OXCs using 3D analog MEMSs allow for a large number of ports. There have been a considerable number of successful systems employing analog MEMSs.[16–21] In most of these systems, however, a precise control of the micromirrors is required. In some cases, tilting accuracies of tens of microradians are necessary.[20,21] As the number of ports increases, so does the complexity of the required control system to direct a signal to any possible output. A simpler control system will facilitate the implementation of a higher number of ports in 3D architectures. To the best of our knowledge, no systems have been implemented using a digital MEMS in 3D architectures, which may have the advantage of simplifying the control system while conserving a high number of ports.

A new approach to the OXC problem was previously proposed.[22,23] Our approach is an OXC architecture with a 3D free-space system while still using digital MEMSs, thus allowing a high number of ports with a relative simpler MEMS control system. Our concept is based on the White cell, a system of three

The authors are with the Department of Electrical and Computer Engineering, Ohio State University, 205 Dreese Laboratory, 2015 Neil Avenue, Columbus, Ohio 43210-1272. V. Argueta-Díaz's e-mail address is argueta-diaz.1@osu.edu.

Received 6 May 2005; revised 7 November 2005; accepted 15 January 2006; posted 17 January 2006 (Doc. ID 61962).

0003-6935/06/194658-11$15.00/0

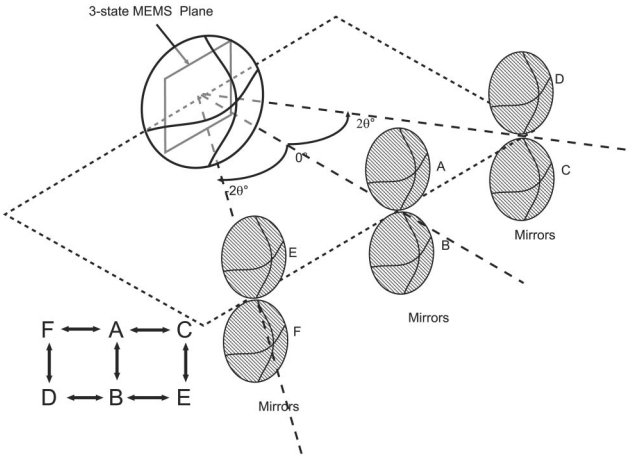

Fig. 1. Quartic OXC based on a three-state MEMS.

spherical mirrors between which light circulates an arbitrary number of times. In the White cell, beams are refocused to spots on each pass. We will arrange these spots to land on the individual pixels of a MEMS tilting micromirror array, and thus have the opportunity to switch a beam toward a new destination on each pass.

Here we present an experimental demonstration of the quartic White cell OXC configuration. In Section 2 we review the quartic White cell OXC and how the system can be simplified for a proof-of-concept system. In Section 3 we present the design considerations and system specifications. In Section 4 simulations of the system and analyses of the beam quality in terms of aberrations are shown. In Section 5 the experimental results of our system are introduced. In Section 6 we present the summary and conclusions of our research.

2. Quartic White Cell Optical Cross-Connect Configuration

Our OXC system is based on the optical White cell.[24,25] The White cell is an arrangement of spherical mirrors that can provide multiple bounces for a large number of input beams that are refocused on every bounce. Each beam forms a unique set of spots. Our goal is to perform optical switching, which we will do by allowing several input beams to be switched among several different White cells. One White cell maintains the beam spots in their current rows (null displacement), whereas the other White cells cause various displacements of the beam position at the MEMS plane.

Figure 1 shows how we might assemble several White cells. Let us suppose we are using a tip–tilt micromirror array in which each pixel has three stable states, and let us take these states to be 0° (flat), $+\theta$, and $-\theta$. Here we place our null cell mirrors (A and B) on the axis normal to the MEMS mirror plane, but one is directly above the other. When the pixels are flat, light goes back and forth between A and B, creating an unshifted spot pattern; hence the null cell. If a pixel is tipped to $+\theta$, light reflects off the MEMS mirror at an angle of 2θ, and we place two more spherical mirrors (D and C) here. Similarly, we place two mirrors (E and F) along the -2θ axis for when the pixel is tipped to $-\theta$.

Figure 1 also shows the allowed transitions. In this case, light from D can go to B (pixel at $+\theta$), or to mirror F (pixel flat). Similarly light can go from C to A, or C to E. As can be seen, light goes from an upper mirror to a lower mirror and vice versa. It is also not possible for light to go directly from C to D, nor from E to F.

We observe that there are two loops in the connectivity diagram, and that each loop is closed. As mentioned above, mirrors A and B produce no shift; thus both are considered to be the null cell. On the other hand, mirrors C, D, E, and F each produce a different specific shift that will be chosen depending on the number of times a beam is allowed to bounce on each of them. We can visit either upper mirror on every other bounce, which we allow up to $m/4$ times. Thus we assign the shift of mirror C to be one row, and the shift produced by mirror E to be $(m/4) + 1$ rows. Since each of these can be visited up to $m/4$ times, the maximum possible shift that can be obtained in m bounces is

$$N_{\text{quartic}} = \left[\left(\frac{m}{4}\right) + 1\right]^4 - 2. \tag{1}$$

References 22 and 23 give a detailed explanation of the OXC systems based on the White cell.

To prove the feasibility of the quartic White cell OXC, we built a simplified version of the system, which we call an underpopulated quartic cell meaning that it has the structure and connectivity of a quartic cell, but with fewer spherical mirrors. The underpopulated quartic cell is shown in Fig. 2. As in the original quartic cell, we have a null cell formed by spherical mirrors A, B, and the MEMS. Even though mirrors D and F are missing, the underpopulated quartic cell is a convenient way to prove that a beam can bounce between the null cell and the lateral arms without fully implementing all the allowed transitions. As can be seen, we are using three field lenses instead of one; this does not affect the bounce pattern of the beams, and also reduces the final size of the field lenses.

A clear feature of the White cell OXC approach is that the number of possible outputs depends on the number of bounces in the White cell. This may be a problem due to the losses caused by the system and the reflectivity of the MEMS micromirror. This problem can be solved either by increasing the reflectivity of the micromirrors or by using other White cell configurations of an OXC so that a lower number of bounces will provide us with a comparable or even higher number of possible outputs.

For example, from Eq. (1) for the quartic cell, the number of possible outputs is proportional to $(m/4)^4$, which will provide 1294 possible outputs in 20 bounces. We refer the reader to Ref. 26 where some specifics about the mirror progressions are given.

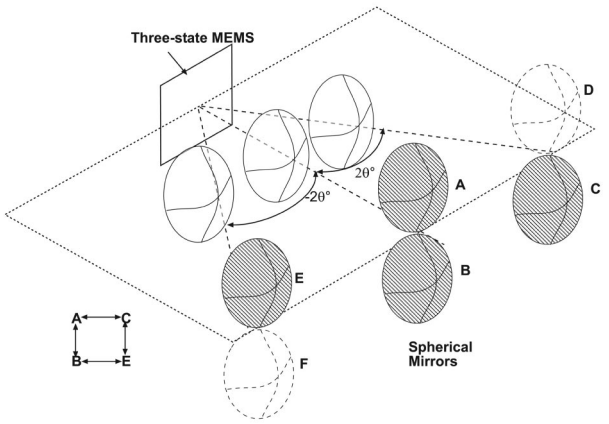

Fig. 2. Underpopulated quartic White cell OXC.

More interesting architectures can be designed if we allow the micromirrors to be tilted in two different planes (up–down, left–right). With such a micromirror one can address up to 6399 outputs with only 17 bounces.[22] Also, the White cell approach allows for a different family of OXCs where the number of bounces correspond to X^m, where X is a given base. In particular, we present a $2^{m/4}$ OXC system design in Ref. 23 where, although the number of possible outputs is lower than in the quartic White cell OXC configuration, this family of systems may offer other kinds of advantage (i.e., add–drop wavelength multiplexer, beam splitting), that are the subjects of current research.

A drawback of our White cell approach, however, is the number of necessary micromirrors. The number of pixels goes up to $(m/2)N^2$. This means that the White cell approach as described here will ultimately require larger MEMSs with more micromirrors than 2D or traditional 3D approaches. The good news is that this introduces redundancy.

We show in Section 3 that there are multiple paths by which a given input can reach a given output. Thus if a pixel fails, other back-up paths exist to reach. In traditional free-space OXC devices, to the best of our knowledge, if a micromirror fails, that connection is no longer possible. It is also true that by reducing the redundancy for all outputs (i.e., having only two redundant paths instead of three or more back-up paths) it will be possible to have a much lower number of micromirrors.

3. Apparatus and Design

We present the spot pattern of an eight-output system in Fig. 3 to illustrate the operation of the underpopulated quartic White cell. Four beams are introduced into the White cell OXC via an input turning mirror (ITM). Normally the number of inputs is chosen to be equal to the number outputs; they are different here solely for experimental convenience. Each beam hits the ITM in a specific position: w, x, y, and z. The MEMS is divided into a grid of nine rows (for eight possible output locations, plus the input row) and three columns. Each cell on this grid is a group of four micromirrors, so that each of the four beams lands on a different micromirror on each bounce. Each beam, therefore, can be independently directed either to the null cell or to spherical mirrors C or E. Every time we go to C we will have a shift of Δ, whereas each time a beam goes to E it will have a shift of 3Δ in the MEMS plane.

Figure 3 shows several bounce patterns for different input positions. Initially all four input beams start in the row at the bottom of the MEMS. We divide the bounce patterns of the four beams into two parts for better understanding. In Fig. 3(a) we show the bounce pattern for two beams that are directed to outputs 0 and 1. The "black" beam is sent to output 0, so the beam bounces only between mirrors A and B, the null cell. The "light gray" beam is sent to output 1; to do so we need to send the beam to mirror C one time. This is done in the third bounce.

Figure 3(b) shows the bounce pattern of the two remaining beams, the "white" and "dark gray" beams. We assume that we need to send the white beam to the fifth output. Therefore we will need to send the white beam to mirror E one time (3Δ displacement) and to mirror C two times (Δ displacement each time). The white beam starts bouncing in the AB White cell (i.e., the micromirrors on the MEMS are tilted to the $-0°$ position), until the second bounce, when the micromirror is tilted to $+\theta$ and the beam is sent to mirror E. Then mirror E will send the white beam back to the MEMS on the third row instead of the zeroth row. We then send the white beam to mirror C, where the beam will be shifted an additional row. We send the white beam to mirror C once again at the fifth bounce, so the beam after seven bounces will come out at the fifth output. In a similar way, we can send the dark gray beam to the fourth output. Figure 3(c) shows the combined bounce patterns of the four beams to their respective outputs.

An important problem to mention about the proposed system is how the beams arrive at the output planes. Figure 4 shows two beams at their final bounce arriving at different outputs. Each beam arrives from different spherical mirrors; while the gray beam comes from mirror B, the white beam comes from mirror E. The fact that each beam comes from different spherical mirrors and goes to different outputs causes the beams to arrive at the output plane with different angles. A serious factor that can affect coupling into a fiber.

There are actually two angles of concern here. The first has to do with from which spherical mirror a beam arrives when it reaches the output region. The other angle arises from the particular output location within that output region in which the spot forms. The first angle is the most severe. Figure 4(a) shows the last bounce for two different beams. The white beam is assumed to be coming from mirror E. On the other hand, the gray beam comes from mirror C on its last bounce. One simple way to solve this problem (difference of angle on which mirror the beam comes from) is to add one additional bounce. Then regard-

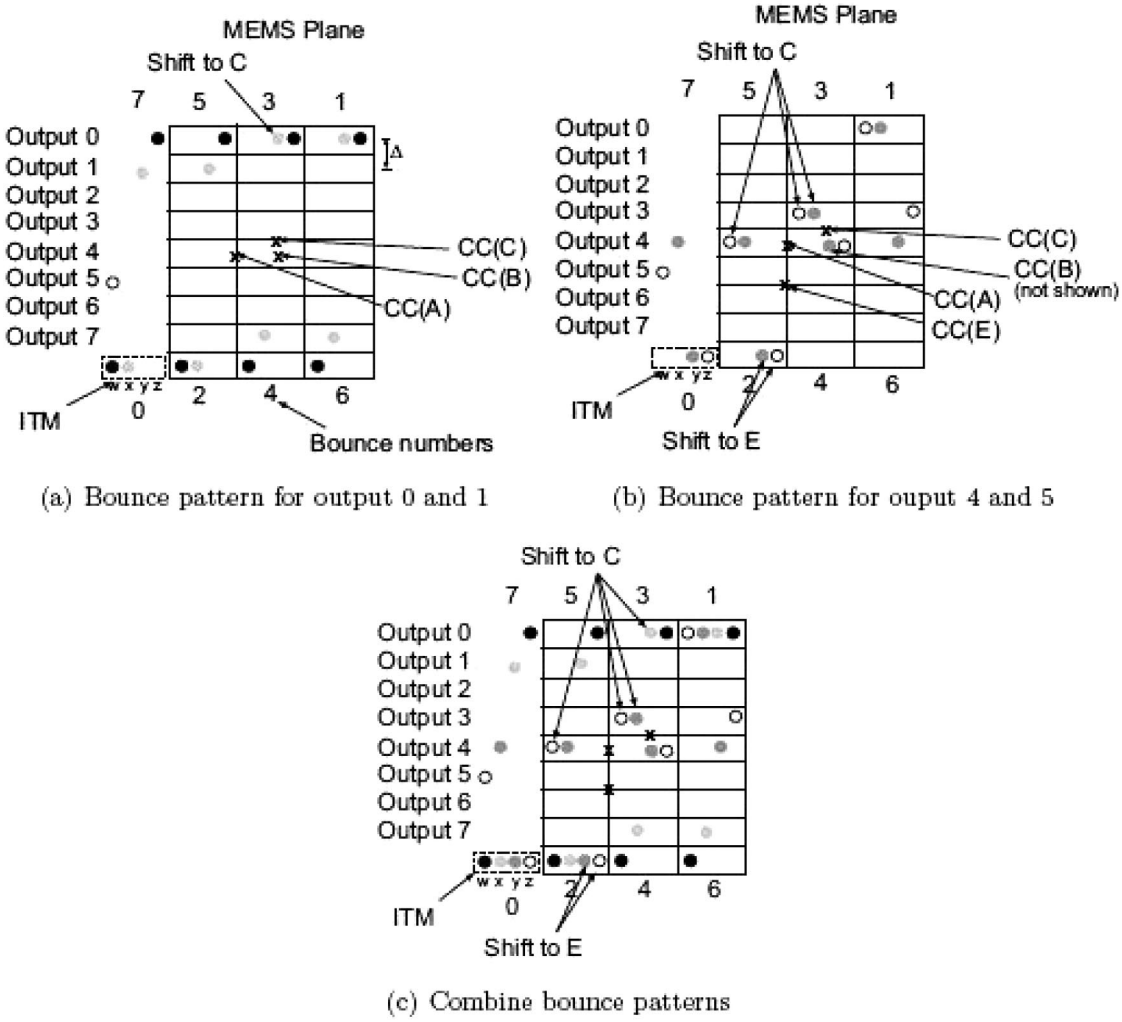

(a) Bounce pattern for output 0 and 1

(b) Bounce pattern for ouput 4 and 5

(c) Combine bounce patterns

Fig. 3. Spot patterns for multiple inputs in the quartic White cell-based OXC.

less of the output selected, each beam can be sent back to the null cell (mirrors A and B) on its last bounce. Now all beams will arrive at their respective output regions from the same general direction, as shown in Fig. 4(b). The beams all arrive from the same White cell now but are still directed to different outputs. Within each output region, each beam may arrive at any of several different locations (e.g., lower corner, middle). This also creates a small difference in the angle at which a beam arrives. This small angle can be important when coupling into fiber. Furthermore the input spot array may be two-dimensional, having both columns and rows. Therefore all the rows and columns must be combined into a single spot, and this must be done taking into account the varying angles of incidence. The output should be a single spot of the same size and shape as any individual input spot, and the output should emerge at a specific angle, independent of the arrival angle of any particular beam. To solve this second angle of incidence we have proposed a beam combiner,[22] but its design and implementation are left for further development.

4. Simulations

Here we present OSLO simulations corresponding to the underpopulated quartic White cell. The objective is to identify whether there is any correlation between the output position of the beam and the aberrations observed. For these simulations the null cell uses a 400 mm focal length BK7 meniscus lens for the field lens. Both lateral wings have a 350 mm focal length BK7 meniscus lens. All spherical mirrors have a 609.8 mm radius of curvature. The beam spot size radius at the MEMS plane is $w_0 = 5$ μm. We are assuming a three-state MEMS with tilting angles of $\pm 10°$ and 0°, and a pitch $\Delta = 250$ μm. The wavelength is $\lambda = 1.55$ μm.

Figure 5 shows the bounce pattern and ray trace analysis when the input in position z on the ITM is sent to the zeroth output. To direct a beam to the zeroth output means that there is no change in the position of the beam; that is, the beam bounces exclusively between mirrors A and B (the null cell). Figure 5(a) shows the bounce pattern for this output. Figure 5(b) shows the corresponding ray trace anal-

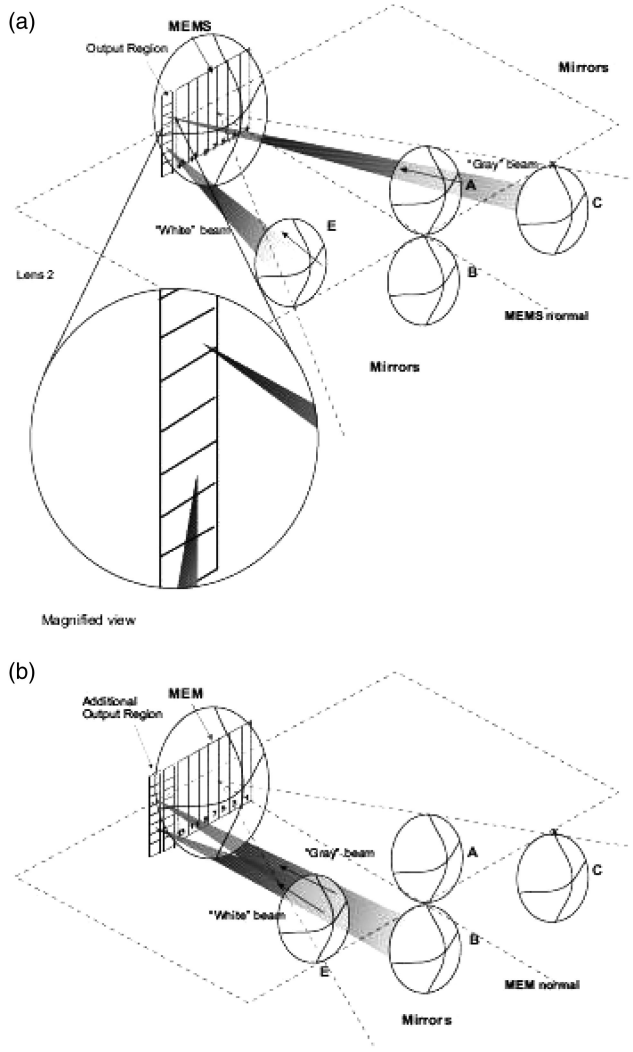

Fig. 4. Last bounce toward the output plane. (a) Beams arriving from different White cell mirrors arrive at different angles. (b) Additional bounce force beams to get to output plane from the same White cell mirror.

ysis. Because the beam bounces exclusively between A and B, the lateral field lenses are not involved in the simulation and therefore are not shown. From the ray intercept curves we can appreciate that the main aberration is astigmatism with a small amount of coma. The astigmatism was found to be only 0.477 782 mm after seven bounces.

Figure 6, on the other hand, shows the bounce pattern and ray trace analysis when the beam in the w input is sent to the seventh output. The bounce pattern of the system is shown in Fig. 6(a). For clarity we placed the bounce number next to the beam spot. In the figure we can see that the beam first bounces in the null cell (bounces 1 and 2); after mirror B the beam is sent to mirror E on bounce 3, which produces a shift of 3Δ, placing the beam on the row corresponding to the third output. We sent the beam to mirror C on bounce 4, which produces an additional shift of Δ. After mirror C we sent the beam again to mirror E on bounce 5, shifting the beam another 3Δ; the two remaining bounces are made on the null cell, thus directing the beam to the seventh output.

Figure 6(b) shows the ray trace analysis for the seventh output. We can appreciate that there is little difference compared to the ray trace analysis for the zeroth output. The seventh output is expected to be the worst case because the beam has to go three times to the lateral arms so the effect of the astigmatism due to the tilt of the spherical mirrors should be more severe. By comparing Figs. 5 and 6, we see that the beam exhibits almost the same amount of aberration to that of zeroth output. We verified that the astigmatism found in the rest of the outputs (one to six) was between these two values. The reason for this is that the tilt angles of the four spherical mirrors are similar, so there is not much difference among the different optical paths for the different outputs. The astigmatism predicted for the seventh output is 0.5934 mm.

We expect, however, that as the port count increases (our example is a comparatively small eight-output system), larger shifts will be required, and there will be a difference in the amount of astigmatism that some optical elements may add to the system. That is, for longer displacements on the MEMS plane, a bigger tilt angle may be required for some of the spherical mirrors, thus increasing the effect of aberrations in the output beams.

We can conclude that the amount of astigmatism depends on the number of times that the beam is sent to the lateral arms (being indistinguishable whether the beam is sent to mirror C or E). The astigmatism is accumulated at each bounce, so there is a limit to the amount of bounces that we can perform before the aberrations cause severe coupling loss. For large port-count systems, the spherical mirrors can be made with toric curvature to correct the astigmatism.

Besides calculating the astigmatism, we want to see if there is any effect on the coupling efficiency. To calculate this dependence we use the OSLO fiber coupling feature. The fiber is assumed to be a single mode fiber normally aligned to the focal point at the output plane. From these simulations we found that coupling losses are lower than 0.2 dB for each case. In general we need to keep a diffraction limited spot size to maximize the coupling efficiency. The White cell configuration keeps a well-focused beam, so that the losses in the system will come from the nonperfect reflectivity of the MEMS micromirrors and the fiber alignment at the output plane.

In general if the astigmatism is less than the depth of focus, we can neglect it. For this system, the depth of focus is 0.91208 mm, compared to a worst-case astigmatism of 0.5934 mm. The criteria for an acceptable beam is ultimately dependent on the summation of all the optical aberrations being smaller than the depth of focus.

5. Experimental Results: Underpopulated Quartic White Cell Optical Cross Currents

We designed and implemented a physical setup as a proof of concept for the quartic cell. We will describe

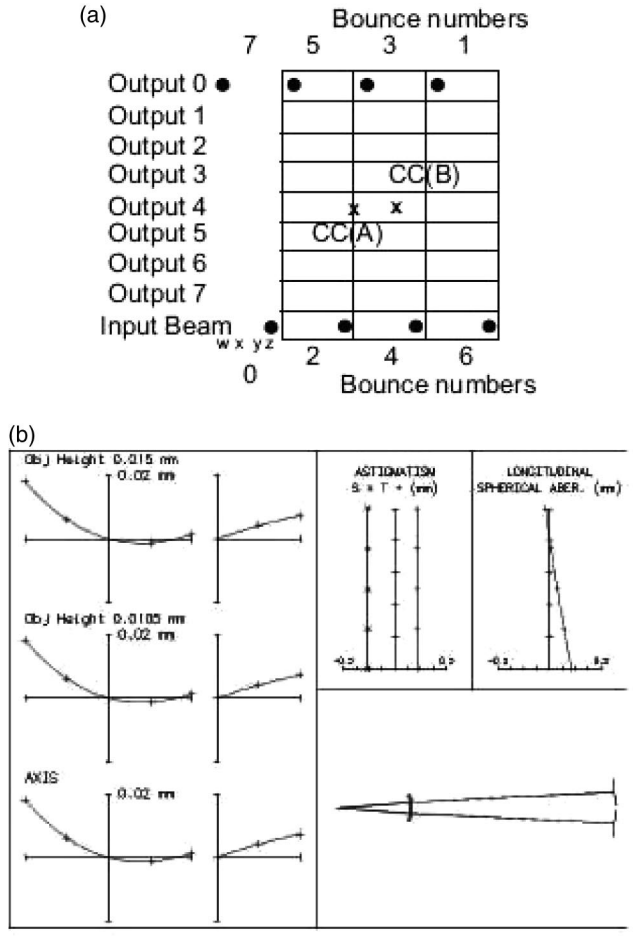

Fig. 5. (a) Bounce pattern and (b) ray trace curves for the zeroth output for the underpopulated quartic OXC.

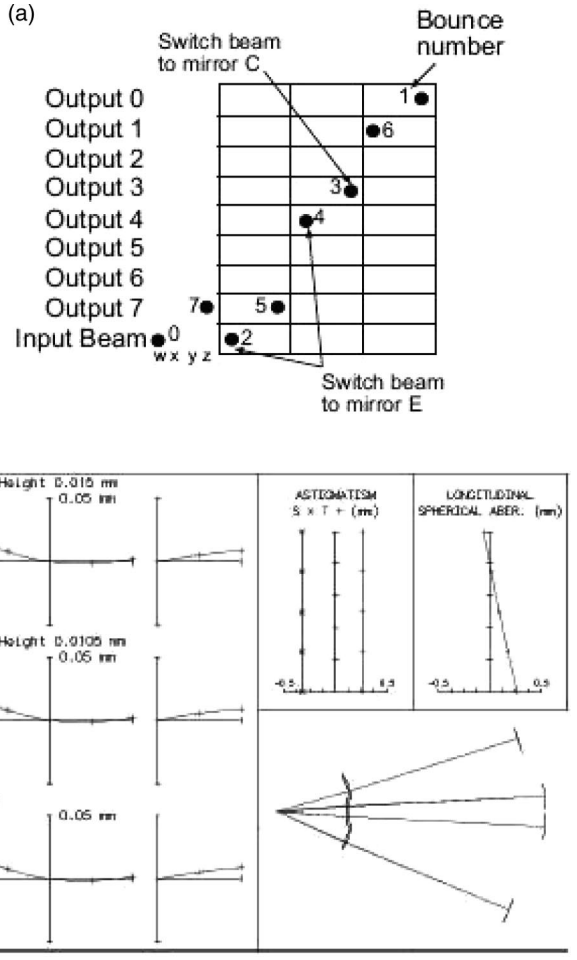

Fig. 6. (a) Bounce pattern and (b) ray trace curves for the seventh output for the underpopulated quartic OXC.

the apparatus, show the bounce patterns obtained for each different output, and demonstrate the switching capabilities of the system. We set up a 4×8 (four inputs, eight outputs) underpopulated quartic cell as our experimental system as shown in Fig. 7. In Fig. 7 at left, we see the pseudo-MEMS (which will be described in Subsection 5.A); in the middle of the figure we can see the three different field lenses (for the null cell and the two lateral arms). Finally, at right in Fig. 7 we can see the four spherical mirrors.

We use spherical mirrors with a radius of curvature of 609.8 mm (Edmund Optics NT43-548 enhanced aluminum). The field lens for the null cell has a focal length of 400 mm (Melles Griot LMP035 uncoated), while the lateral field lenses have focal lengths of 350 mm (Melles Griot LMP031 uncoated). All the optical elements have a 50.8 mm diameter and are made from BK7 glass ($n = 1.50056$ at 0.6328 μm).

An important element of our experimental setup is the MEMS. Because of budget restrictions, it was not possible to get a proper MEMS. Instead we designed and fabricated what we call a pseudo-MEMS, which is described in Subsection 5.A.

A. Pseudo Microelectromechanical Systems

For our setup we use what we call a pseudo-MEMS. The main function of the psuedo-MEMS is to serve as a substitute for a regular MEMS by imitating the tilting function of individual mirrors. The main differences between our pseudo-MEMS and a proper MEMS are the size of the micromirrors and how the tilting of the micromirrors is controlled.

A drawing of the pseudo-MEMS is shown in Fig. 8. A box was constructed that can hold rectangular segments, each of which has a mirrored top. Some of the tops are tilted to 10° and some are flat. The case can hold up to 12 columns (A–L), each column with nine rows (0–8). This gives a total of 108 positions where we can place individual rectangular pieces. Position (A, 0) is located in the upper left-hand corner, while position (L, 8) is in the lower right-hand corner.

The rectangular pieces are shown in Fig. 8(b). Each rectangular piece has a dimension of 0.0625 in. (0.16 cm) × 0.0625 in. (0.16 cm) × 0.50 in. (1.27 cm). Each piece is used to simulate a micromirror, so each piece has a segment of reflective material glued to its top. The rectangular pieces are interchangeable, so it is possible to create a specific bounce pattern by placing the rectangular pieces with the required angles in the

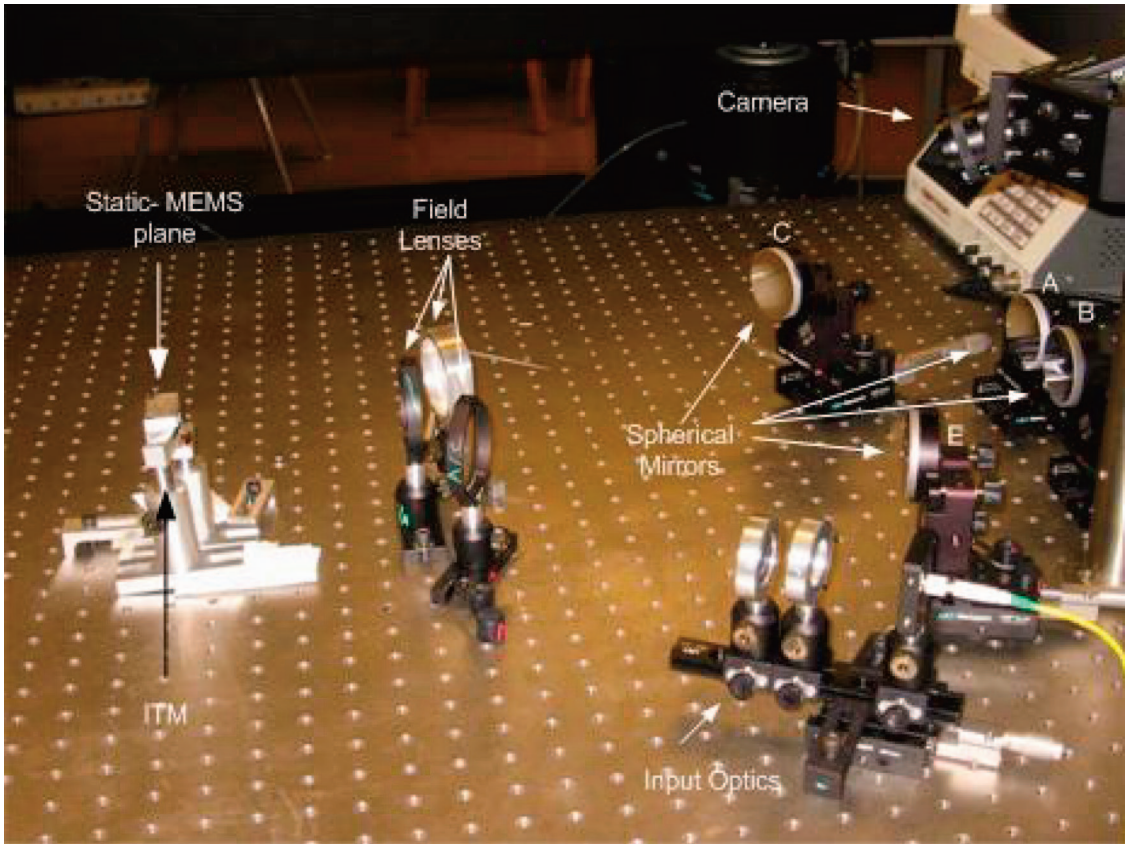

Fig. 7. (Color online) Experimental setup for underpopulated quartic cell OXC.

correct positions. In Subsection 5.B we explain in more detail how we can modify the bounce pattern and direct a beam to specific outputs.

As mentioned before a piece of reflective material is placed on top of the rectangular pieces. We chose small pieces of a silicon wafer cut to the correct size, i.e., 0.0625 in. (0.16 cm) × 0.0625 in. (0.16 cm). Silicon was chosen because it is relatively easy to cut with the required precision to the required size by use of a dicing saw. Since it is uncoated, however, its reflectivity is poor.

Another drawback to using a pseudo-MEMS is that

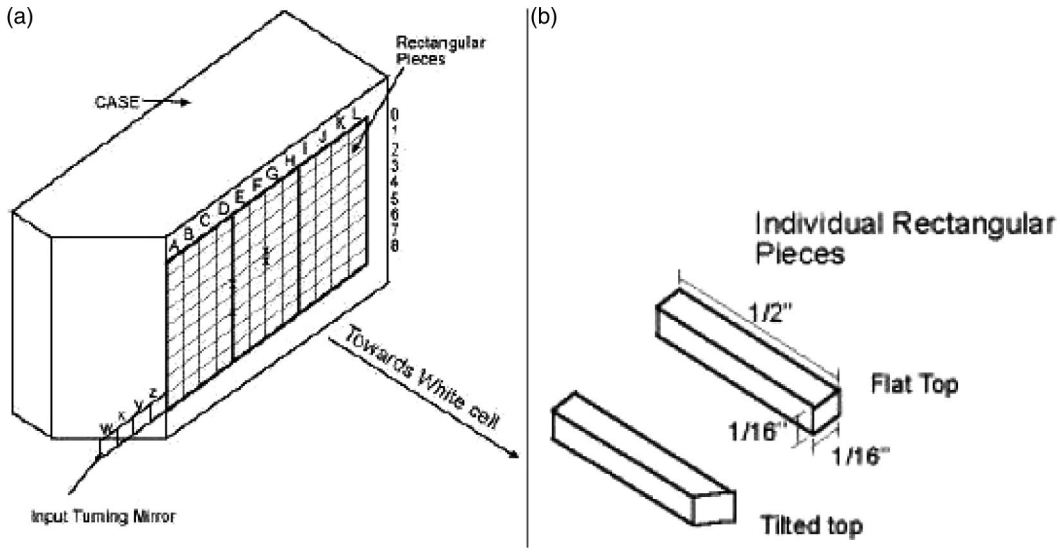

Fig. 8. Schematics of (a) pseudo-MEMS and (b) individual rectangular pieces with a flat top and a tilted top.

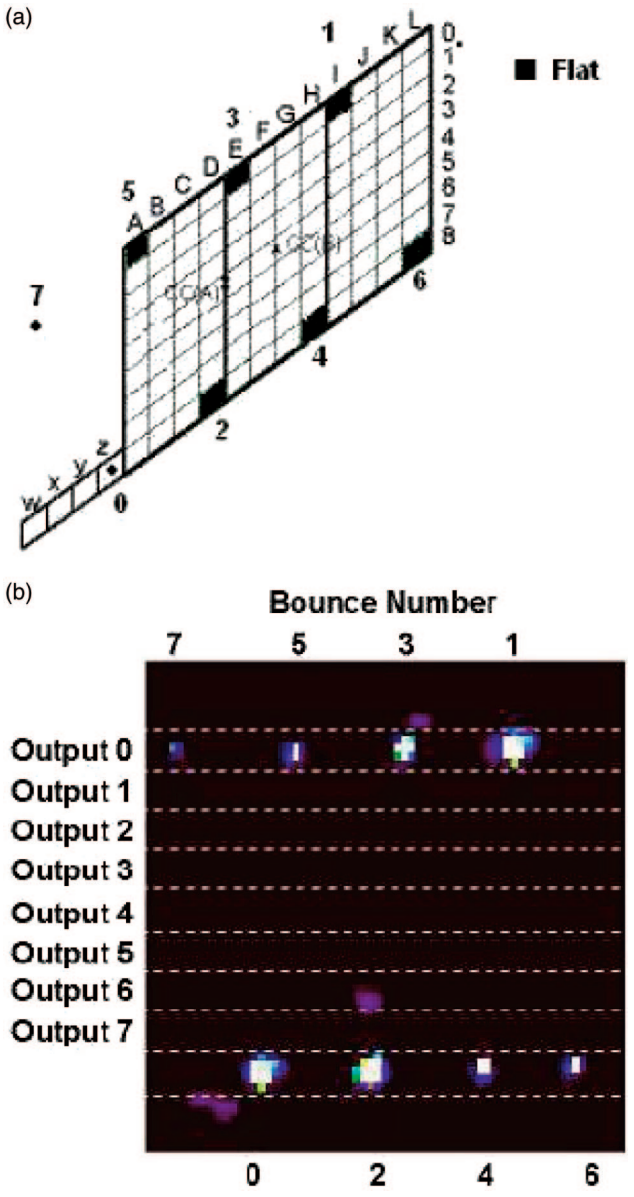

Fig. 9. (Color online) (a) Bounce pattern on pseudo-MEMS plane for zeroth output on the underpopulated quartic White cell OXC. (b) Photograph of bounce pattern at pseudo-MEMS.

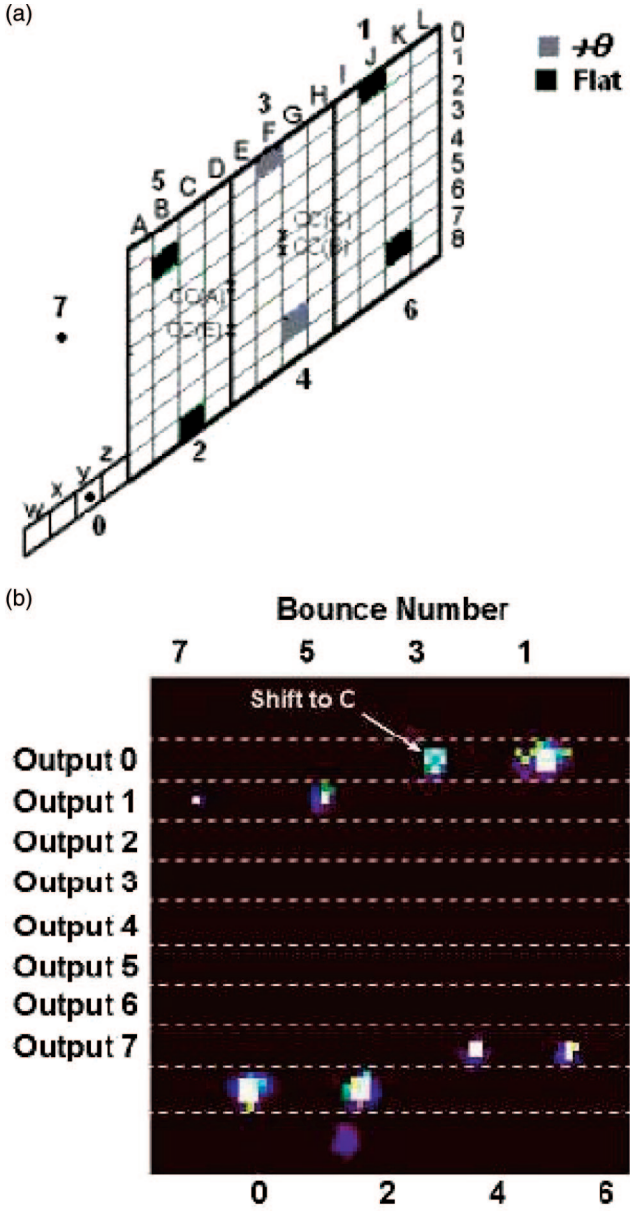

Fig. 10. (Color online) (a) Bounce pattern on pseudo-MEMS plane for first output on the underpopulated quartic White cell OXC. (b) Photograph of bounce pattern at pseudo-MEMS.

we are not able to observe the effects of diffraction that would be observed from the edges of the micromirrors in a proper MEMS. Also, the achievable flatness in a proper MEMS may affect the different beams after several bounces. We have, however, designed and implemented several White cell systems where several bounces have been performed with success.[22,27–29]

B. Bounce Patterns

Figure 9 shows the bounce pattern for a beam that is directed to the zeroth output. The beam is introduced into the White cell by reflecting on position z of the ITM. From the ITM, the beam is sent to spherical mirror A; the center of curvature of mirror A is set in such a way that the reflected beam is sent to position (I, 0) on the pseudo-MEMS on the first bounce. The rectangular piece at position (I, 0) now has a flat top, indicated by the black color, so the beam is sent to spherical mirror B. Light reflected from B is sent to position (D, 8) on the second bounce. The rectangular piece in this position also has a flat top, so the beam is sent again to mirror A. The beam lands on position (E, 0) on the third bounce, on (H, 8) on the fourth bounce, (A, 0) on the fifth bounce, (L, 8) on the sixth bounce, and finally the beam goes to position (w, 0) outside the pseudo-MEMS on the seventh bounce. The bounce pattern describes two parallel lines as expected. Figure 9(b) shows the actual bounce pattern on the pseudo-MEMS taken by a camera.

Figure 10 shows a bounce pattern to send a beam to the first output. This time the beam is introduced into the White cell by reflecting a beam in position y on the

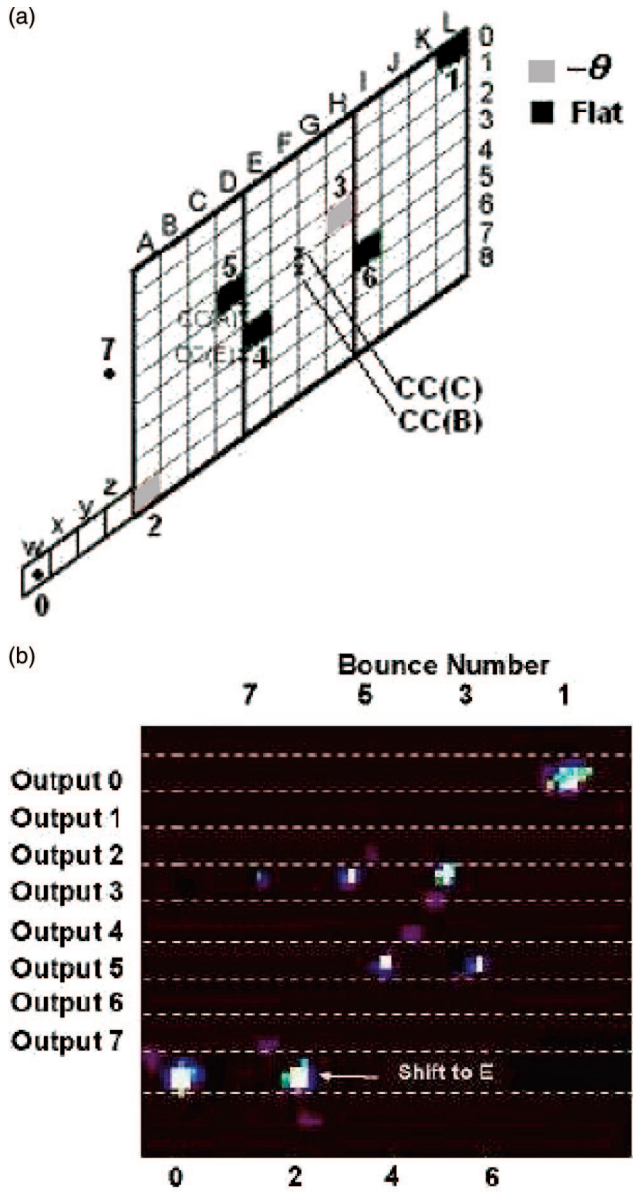

Fig. 11. (Color online) (a) Bounce pattern on pseudo-MEMS plane for (b) third output on the underpopulated quartic White cell OXC.

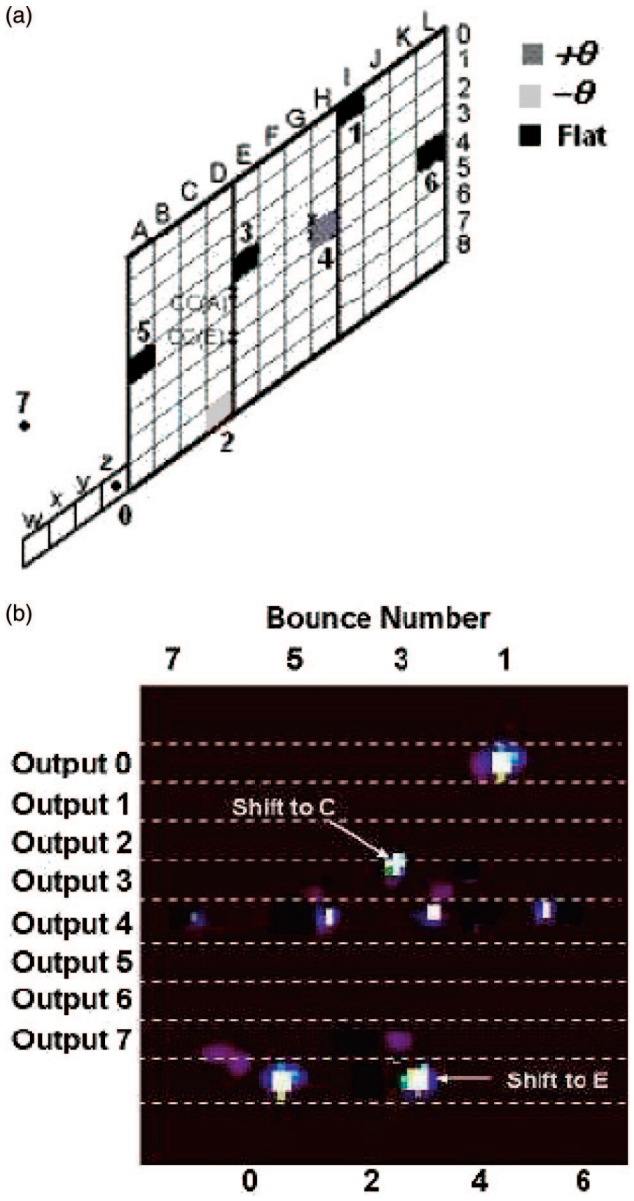

Fig. 12. (Color online) (a) Bounce pattern on pseudo-MEMS plane for (b) fourth output on the underpopulated quartic White cell OXC.

input turning mirror. The beam is then reflected toward spherical mirror A. In this case, the beam from spherical mirror A is sent to position (J, 0), which has a flat top, so the beam is sent to spherical mirror B (bounce 1). The beam bounces back and forth between mirror A and B until it reaches position (F, 0), which has a +10° tilted top, indicated by the gray color, sending the beam to spherical mirror C (bounce 3). After going to mirror C the beam lands on the pseudo-MEMS on position (G, 7). In this position the rectangular piece also has a tilted top to +10°; thus the beam will be reflected toward spherical mirror A (bounce 4). The remaining bounces happen exclusively between spherical mirrors A and B. Finally, the beam leaves the pseudo-MEMS on position (x, 1).

We must note that even though we send the beam to spherical mirror C on bounce 3, we could have sent it there on bounce 1 or bounce 5 and still reached the same output. Thus if a pixel on a real MEMS should fail, the quartic OXC is inherently redundant and the MEMS does not need to be replaced. There are alternative paths to the same output.

In order to send a beam to the third output we send the beam one time to spherical mirror E, which produces a 3Δ shift in the beam's next position. Figure 11 shows one possible configuration to reach this output. The beam is introduced to the White cell by bouncing in position w on the ITM. The first two bounces are done in the null cell: from (A, 8), which has a −10° tilted top, represented by the light gray color. The beam is sent to spherical mirror E (bounce 2), shifting the beam position by 3Δ. The beam from spherical mirror E is thus sent to position (H, 3) on the pseudo-

MEMS. From (H, 3) the beam is sent to spherical mirror A (bounce 3) by placing a $-10°$ tilted top rectangular piece. The remaining bounces happen exclusively in the null cell. The beam leaves the pseudo-MEMS on position (z, 3).

To send a beam to the fourth output it is necessary to send the beam one time to mirror C (Δ), and one time to mirror E (3Δ) as shown in Fig. 12.

To send a beam to output 5 we need to send the beam one time to mirror E and two times to mirror C. To send a beam to output 6 we need to send the beam two times to mirror E, and to send a beam to output 7 we need to send the beam two times to mirror E and one time to mirror C. The bounce pattern for each output is not shown for brevity.

The bounce patterns shown in this section prove that our system can alternate among the central and the lateral arms in the underpopulated quartic cell. We have shown that it is possible to control the output destination by using a three-state MEMS.

C. Loss

It can be seen in Figs. 9–12 that there is a distinct decrease in the size of the spots. The reason for this is that some of the field lenses, as well as the silicon used as reflective surfaces in the pseudo-MEMS, did not have any antireflection coatings, so the losses in the system are considerable. The lack of antireflection coating is also to blame for the presence of ghost images. In a different project, where we used the coated optics in a similar White cell architecture, but for true time delays instead of an interconnection device, we measured a loss of 0.5 dB for the null cell, 4.4 dB for arm C, and 4.4 dB for arm E after ten bounces.[27] There is no reason to assume that the losses observed in Ref. 27 could not be translated to an OXC system based in the same White cell configuration.

D. Redundancy

The redundancy in the White cell is a clear advantage of this architecture. As mentioned in Subsection 5.D, a particular beam has several possible paths to get to the same output. For example, in the case of a beam trying to get to the first output, the beam can be directed to spherical mirror C in the first bounce, the third bounce, or the fifth bounce. Thus for this particular output three alternate paths exist. For the fourth output there are nine possible paths available. The number of possible paths for a given output in the underpopulated quartic cell is given by

$$P_{\text{underquartic}} = \begin{bmatrix} \frac{m}{2} \\ C \end{bmatrix} \begin{bmatrix} \frac{m}{2} \\ E \end{bmatrix}, \tag{2}$$

where $P_{\text{underquartic}}$ is the number of possible paths and $\begin{bmatrix} \frac{m}{2} \\ C \end{bmatrix}$ and $\begin{bmatrix} \frac{m}{2} \\ E \end{bmatrix}$ are the binomial coefficients of the number of times we need to send a beam to mirror C and E for a particular output in a given number of bounces m, respectively. From Eq. (2) we can see that zero output has only one possible path (bouncing exclusively between mirrors A and B). This can be solved by adding an extra bounce so that there is always one alternate path.

It is important to mention that even though there are several paths for each output, each spot path is unique and thus strikes a unique set of pixels, so even if alternate paths exist for each output, they do not block other existing paths. This can be seen clearly in Fig. 3 on.[22] Redundancy does not exist in traditional 3D optical cross-connect systems; thus if a given pixel fails then one particular input or output is out of commission.

It can also be seen that, as the number of bounces increases, so does the number of back-up paths for each possible output.

6. Summary and Conclusions

We have designed, simulated, and experimentally demonstrated a four input by eight output White cell optical cross-connect system. This system is based on a combination of microelectromechanical systems with an optical White cell. The solution presented has the attractive feature that even though it is a 3D free-space system, thus allowing a high number of possible inputs and outputs, it uses a digital MEMS, which requires a simpler control system. Also, this OXC system is inherently redundant, with multiple paths to the same output, thus increasing reliability.

We presented simulations for the system in Section 4. We found that the aberrations present in each output depend not only on the chosen output but also on the input position of the analyzed beam. In all cases presented we found that the main contribution to aberration comes from astigmatism, and also that the astigmatism for all cases is below the depth of focus of the system.

In Section 5 we realized an experimental setup of an underpopulated quartic White cell. Although two of the spherical mirrors were left out for simplicity, the main objective of the experiments was to prove that it was possible to control the final output of a particular beam by using the tilting mirrors of a MEMS. Due to the lack of a MEMS, we used a pseudo-MEMS, a static arrangement of interchangeable mirrors, whose function is to imitate a proper MEMS. The main difference between our pseudo-MEMS and a proper MEMS is that the micromirrors are controlled manually. We presented the bounce pattern for a beam sent to eight different outputs. The important aspect is that we are able to control the output row by sending the beam to specific spherical mirrors as we predicted.

We thank William Thalgott and Feras Abou Galala for their time and expertise to construct the pseudo-MEMS and cut the silicon wafers, respectively.

References

1. L. Y. Lin and E. L. Goldstein, "Opportunities and challenges for MEMS in lightwave communications," IEEE J. Sel. Top. Quantum Electron. **8,** 163–172 (2002).
2. G. I. Papadimitriou, C. Papazoglou, and A. S. Pomportsis,

"Optical switching: switch fabrics, techniques, and architectures," J. Lightwave Technol. **21,** 384–405 (2003).
3. P. B. Chu, S.-S. Lee, and S. Park, "MEMS: the path to large optical crossconnects," IEEE Commun. Mag. **40**(3)**,** 80–87 (2002).
4. D. J. Bishop, C. R. Giles, and G. P. Austin, "The Lucent lambdarouter: MEMS technology of the future here today," IEEE Commun. Mag. **40**(3)**,** 75–79 (2002).
5. T.-W. Yeow, K. L. E. Law, and A. Goldenberg, "MEMS optical switches," IEEE Commun. Mag. **39**(11)**,** 158–163 (2001).
6. D. K. Probst, L. G. Perrymore, B. C. Johnson, R. J. Blackwell, J. A. Priest, and C. L. Balestra, "Demonstration of an integrated, active 4×4 photonic crossbar," IEEE Photon. Technol. Lett. **4,** 1139–1140 (1992).
7. M. Okuno, K. Kato, R. Nagase, A. Himeno, Y. Ohmore, and M. Kawachi, "Silica-based optical matrix switch integrating new switching units with large fabrication tolerance," J. Lightwave Technol. **17,** 771–780 (1999).
8. M. P. Earnshaw, J. B. D. Soole, M. Cappuzzo, L. Gomez, E. Laskowski, and A. Paunescu, "8×8 optical switch matrix using generalized Mach–Zehnder interferometers," IEEE Photon. Technol. Lett. **15,** 810–812 (2003).
9. T. Goh, M. Yasu, K. Hattori, A. Himeno, M. Okuno, and Y. Ohmori, "Low-loss and high-extinction ratio silica-based strictly nonblocking 16×16 thermooptic matrix switch," IEEE Photon. Technol. Lett. **10,** 810–812 (1998).
10. M. Makihara, "Micromechanical optical switches based on thermocapillarity integrated in waveguide substrate," J. Lightwave Technol. **17,** 14–18 (1999).
11. D. K. Yang, "A simulation study of a liquid crystal optical switch based on total internal reflection," J. Opt. A Pure Appl. Opt. **5,** 402–408 (2003).
12. P. De Dobbelaere, K. Falta, S. Gloeckner, and S. Patra, "Digital MEMS for optical switching," IEEE Commun. Mag. **40**(3)**,** 88–95 (2002).
13. L. Y. Lin, E. L. Goldstein, and R. W. Tkach, "Free-space micromachined optical switches with submilisecond switching time ofr large scale optical cross-connects," IEEE Photon. Technol. Lett. **10,** 525–527 (1998).
14. R. T. Chen, H. Nguyen, and M. C. Wu, "A low voltage micromachined optical switch by stress-induced bending," presented at the 12th IEEE International Conference on Micro Electro Mechanical Systems, Orlando, Fla. (1999).
15. H. Laor, "MEMS mirrors applications in optical crossconnects," in *IEEE LEOS Sum- mer Topical Meetings: Optical MEMS,* Monterey, Calif. (1998).
16. P. M. Hagelin, U. Krishnamoorthy, J. P. Heritage, and O. Solgaard, "Scalable optical cross-connect switch using micromachined mirrors," IEEE Photon. Technol. Lett. **127,** 882–884 (2000).
17. X. Zheng, V. Kaman, S. Yuan, Y. Xu, O. Jerphagnon, A. Keating, R. C. Anderson, H. N. Poulsen, B. Liu, J. R. Sechrist, C. Pusarla, R. Helkey, D. J. Blumenthal, and J. E. Bowers, "Three-dimensional MEMS photonic cross-connect switch design and performance," IEEE J. Sel. Top. Quantum Electron. **9,** 571–578 (2003).
18. D. T. Neilson, R. Frahm, P. Kolodner, C. A. Bolle, R. Ryf, J. Kim, A. R. Papazian, C. J. Nuzman, A. Gasparyan, N. R. Basavanhally, V. A. Aksyuk, and J. V. Gates "256×256 port optical cross-connect subsystem," J. Lightwave Technol. **22,** 1499–1509 (2004).
19. O. Jerphagnon, R. Anderson, A. Chojnacki, R. Helkey, W. Fant, V. Kaman, A. Keating, B. Liu, C. Pusaria, J. R. Sechrist, D. Xu, S. Yuan, and X. Zheng, "Performance and applications of a large port-count and low-loss photonic cross-connect systems for optical networks," in *the 15th Annual Meeting of the IEEE Lasers and Electro-Optics Society LEOS* **1,** 299–300 (2002).
20. J. Kim, C. J. Nuzman, B. Kumar, D. F. Lieuwen, J. S. Kraus, A. Weiss, C. P. Lichtenwalner, A. R. Papazian, R. E. Frahm, N. R. Basavanhally, D. A. Ramsey, V. A. Aksyuk, F. Pardo, M. E. Simon, V. Lifton, H. B. Chan, M. Haueis, A. Gasparyan, H. R. Shea, S. Arney, C. A. Bolle, P. R. Kolodner, R. Ryf, D. T. Neilson, J. V. Gates, "1100×1100 port MEMS-based optical crossconnect with 4-dB maximum loss," IEEE Photon Technol. Lett. **15,** 1537–1539 (2003).
21. J. I. Dadap, P. B. Chu, I. Brener, C. Pu, C. D. Lee, K. Bergman, N. Bonadeo, T. Chau, M. Chou, R. Doran, R. Gibson, R. Harel, J. J. Johnson, S. S. Lee, S. Park, D. R. Peale, R. Rodriguez, D. Tong, M. Tsai, C. Wu, W. Zhong, E. L. Goldstein, L. Y. Lin, and J. A. Walker, "Modular MEMS-based optical cross-connect with large port-count," IEEE Photon. Technol. Lett. **15,** 1773–1775 (2003).
22. B. L. Anderson, V. Argueta-Diaz, F. Abou-Galala, G. Radhakrishnan, and R. J. Higgins, "Optical cross connect switch based on tip/tilt micromirrors in a White cell," IEEE Sel. Top. Quantum Electron. **9,** 579–593 (2003).
23. V. Argueta-Diaz and B. L. Anderson, "Reconfigurable photonic switch based on a binary system using the White cell and Micromirror Arrays," IEEE J. Sel. Top. Quantum Electron. **9,** 594–602 (2003).
24. J. U. White, "Long optical paths of large aperture," J. Opt. Soc. Am. **32,** 285–288 (1942).
25. J. U. White, "Very long optical paths in air," J. Opt. Soc. Am. **66,** 411–416 (1976).
26. B. L. Anderson and R. Mital, "Polynomial-based optical true-time delay devices using MEMs," Appl. Opt. **41,** 5449–5461 (2002).
27. C. M. Warnky, R. Mital, V. Argueta-Díaz, and B. L. Anderson, "Demonstration of a quartic cell, a free-space true-time delay device based on the White cell," submitted to J. Lightwave Technol.
28. A. Rader and B. L. Anderson, "Demonstration of a linear optical true-time delay device using a microelectromechanical mirror array," Appl. Opt. **42,** 1409–1416 (2003).
29. R. L. Higgins, N. K. Nahar, and B. L. Anderson, "Design and demonstration of a switching engine for a binary true-time-delay device that uses a White cell," Appl. Opt. **42,** 4747–4757 (2003).